



Comparison of numerical models for bulk and surface acoustic wave-induced acoustophoresis in a microchannel

Yufeng Zhou^a

School of Mechanical and Aerospace Engineering, Nanyang Technological University, Singapore, Singapore

Received: 4 February 2020 / Accepted: 14 August 2020 / Published online: 5 September 2020
© Società Italiana di Fisica and Springer-Verlag GmbH Germany, part of Springer Nature 2020

Abstract Acoustophoresis induced by either bulk or surface acoustic wave has great potential to manipulate microparticles and biological substances because of its simple setup, low power consumption, and high generated force. Numerical models for simulating acoustophoresis in a microchannel are required to further understand the underlying mechanisms (i.e., standing acoustic wave and microparticle motion) and optimize the design. Simplified models that only consider the channel walls as actuation and impedance boundaries are available. In this study, full-sized models were established to include many phenomena and physical interactions involved and then compared with the simulation results using the simplified models. Distributions of acoustic pressure, streaming velocity, radiation force, and trajectory of 1 μm and 10 μm microparticles were calculated for further understanding of acoustofluidics. Overall, the full-sized models can provide an accurate guideline for the application and development of acoustophoresis.

1 Introduction

Acoustofluidics has been emerging as an effective and precise tool for purely mechanical and label-free manipulation of microparticles and cell suspensions in lab-on-a-chip technologies [13, 23, 31]. It is a versatile tool that can address many limitations of other manipulation techniques. When a standing acoustic field is established in a microchannel, the particles are subject to the acoustic radiation force from the scattering of the acoustic waves and the Stokes drag force from the induced acoustic streaming flow. To produce the ultrasonic wave in the acoustofluidic channel one of the methods is the vibration of a piezoelectric material in either the thickness or shear modes, and such ultrasonic waves are referred as bulk acoustic wave (BAW) [10]. The other method developed in recent years is the surface acoustic wave (SAW)-based system. SAWs actuated on a piezoelectric substrate propagate along the surface and radiate into the coupling fluid. Acoustofluidic device can achieve many successful applications, such as separation lipid from blood [11, 24, 28], separation and

Electronic supplementary material The online version of this article (<https://doi.org/10.1140/epjp/s13360-020-00697-x>) contains supplementary material, which is available to authorized users.

^a e-mail: yfzhou@ntu.edu.sg (corresponding author)

concentration of rare tumor cells from white blood cells [1, 30], and continuous separation of mixed particle suspensions into multiple outlet fractions [5, 6, 8, 23]. It has the advantages of simple architecture and high throughputs.

Half-wavelength resonators with laminar flow (low Reynolds number) inside the microchannel have been developed since the 1990s [15, 16]. In the BAW-based transversal resonators, the entire microfluidic component with low acoustic losses but much high acoustic impedance in comparison to that of the fluid is actuated in the transversal mode [14]. Numerical analysis for microparticle acoustophoresis including acoustic radiation force, streaming flow, and boundary layers is required for understanding the underlying mechanism and particle manipulation with better accuracy. However, in comparison to the experimental studies, there is less investigation in numerical modeling. An idealized model, neglecting the chip structure and presenting the silicon-glass chip as hard-wall boundary conditions, was established to calculate the transient motion of particles suspended in a liquid-filled microchannel and driven by the acoustophoretic forces arising from an imposed standing acoustic wave with the inclusion of crucial thermoviscous boundary layer near the rigid wall [17]. Since acoustofluidic resonators encompass both fluid and solid material, and the difference in their acoustic impedance is not very large, a pressure field in the fluid will necessarily give rise to motion and deformations of the solid structure surrounding it. Thus, the influence of the solid materials is very important for the behavior of the resonator, and the numerical modeling in order to understand the system as a whole [7]. In the framework of linear viscoelasticity, the displacement and deformation of the solid resonator were found to be significant in the vertical direction, which suggests that the standing acoustic wave inside the fluidic cavity is strongly influencing the silicon chip. Meanwhile, the piezoelectric transducer was omitted for simplicity reasons in that study. The excitation was described as displacement amplitude in the middle of the silicon bottom over a short length. Impedance boundary conditions were used to model the poly-dimethylsiloxane (PDMS) microchannel walls, and a displacement function based on a numerical study of piezoelectric actuation was implemented to model the acoustic actuation of SAW [18]. The obtained first-order field is a horizontal standing wave that travels vertically from the actuated wall toward the liquid-filled upper wall, from which the acoustic streaming and radiation force acting on suspended particles are calculated similarly as BAW-based system. The position of the vertical pressure node along the channel width could be tuned by the phase difference between the two incident SAWs. Although the low ratio of the transverse to longitudinal speed of sound justifies a fluid-like model of PDMS, treating acoustically soft PDMS as linear elastic materials results in significant differences with the reduced lossy-wall model [27]. Such discrepancies may be due to the negligence of energy leakage from a substrate into the sidewall, the non-planar geometries of PDMS-water boundaries, and the presence of the shear wave in the PDMS. In a recent model [22], the electro-acoustic actuation was included for the generation of SAW instead of using a displacement boundary, but a low-reflecting boundary at the top of the PDMS lid (with a height of only 25 μm) was set, which may be only valid at high frequency. In this work, two full-sized models were established for the calculation of BAW- and SAW-induced acoustophoresis, the former including the piezoelectric material, silicon chip, fluid, and glass lid and the latter including piezoelectric substrate, interdigital transducer electrodes, linear elastic PDMS microchannel, and fluid. Simulation results were then compared with those using the simplified models. The numerical modeling will be helpful in a further understanding of acoustophoresis and device design optimization as well as technological improvements for more accurate and reliable manipulation of microparticles and biological cells.

2 Materials and methods

2.1 BAW-induced acoustofluidics in the microchannel

BAW-induced acoustophoresis in a microchannel with a width of 380 μm and a height of 160 μm was simulated using two models (see Fig. 1). In the simplified model as shown in Fig. 1a, the idealized conditions were applied to the simulation. The chip structure was neglected, and the silicon-glass chip was presented as hard-wall boundaries [17]. In comparison, piezoelectric material (800 μm × 110 μm), silicon chip (580 μm × 260 μm), and glass lid (580 μm × 100 μm) were included in the full-sized model (see Fig. 1b). The microchannel has half-wavelength resonance across its width at the excitation frequency of 1.97 MHz. The motion of microparticles was determined by Newton’s second law

$$m_p \frac{dv_p}{dt} = F_{rad} + F_{drag} \tag{1}$$

where m_p is the mass of a microparticle, v_p is the velocity of the microparticle, F_{rad} is the acoustic radiation force, F_{drag} is the Stokes drag force. F_{rad} is given by [9, 26]

$$F_{rad} = -\pi a^3 \left[\frac{2\kappa_f}{3} \text{Re}[f_1^* p_1^* \nabla p_1] - \rho_w \text{Re}[f_2^* v_1^* \cdot \nabla v_1] \right] \tag{2}$$

where a is the radius of the microparticle, κ_f is the compressibility of the fluid, $\text{Re}(\ast)$ denotes the real part, \ast denotes the complex conjugate, p_1 and v_1 are the first-order acoustic pressure and velocity, respectively.

$$f_1 = 1 - \frac{\kappa_p}{\kappa_f} \tag{3}$$

$$f_2 = \frac{2(1 - \gamma)(\rho_p - \rho_f)}{2\rho_p + \rho_f(1 - 3\gamma)} \tag{4}$$

$$\gamma = -\frac{3}{2} \left[1 + i(1 + \tilde{\delta}) \right] \tilde{\delta}, \quad \tilde{\delta} = \frac{\delta}{a}, \quad \delta = \sqrt{\frac{2\mu}{\omega\rho_0}} \tag{5}$$

where μ is the fluid viscosity, ω is the angular frequency, κ_p is the compressibility of the microparticle, δ is the viscous penetration depth and is equal to 0.38 μm at the resonant frequency of 1.97 MHz, ρ_f and ρ_p are the density of fluid and microparticle, respectively. F_{rad} is given by [12]

$$F_{drag} = 6\pi\mu a(v_2 - v_p) \tag{6}$$

where v_2 is the second-order streaming velocity, $\langle \ast \rangle$ denotes the time average over a full oscillation period.

All simulation was performed using the finite element method (FEM) in COMSOL Multiphysics (v5.4, Burlington, MA). Properties of all materials used in this study are listed in Table S1. In the simplified model, COMSOL modules of thermoacoustics, laminar flow and particle tracing were included. The ultrasonic piezoelectric transducer was presented as the velocity boundary of the lateral actuated walls while the top and bottom walls were rigid walls with no slip boundaries. In comparison, COMSOL modules of thermoacoustics, laminar flow, particle tracing, solid mechanics, and electrostatics were included with the coupling interfaces of the piezoelectric effect and acoustic-structure boundary in the full-sized model. The coupling to the acoustic pressure p and velocity v in the microchannel walls is described by the continuity conditions through the Cauchy model, $n \cdot \sigma_s = n \cdot \sigma_f$ and $\partial_t u = v$, where σ is the stress tensor, n is outward pointing surface normal vector, u is the displacement of

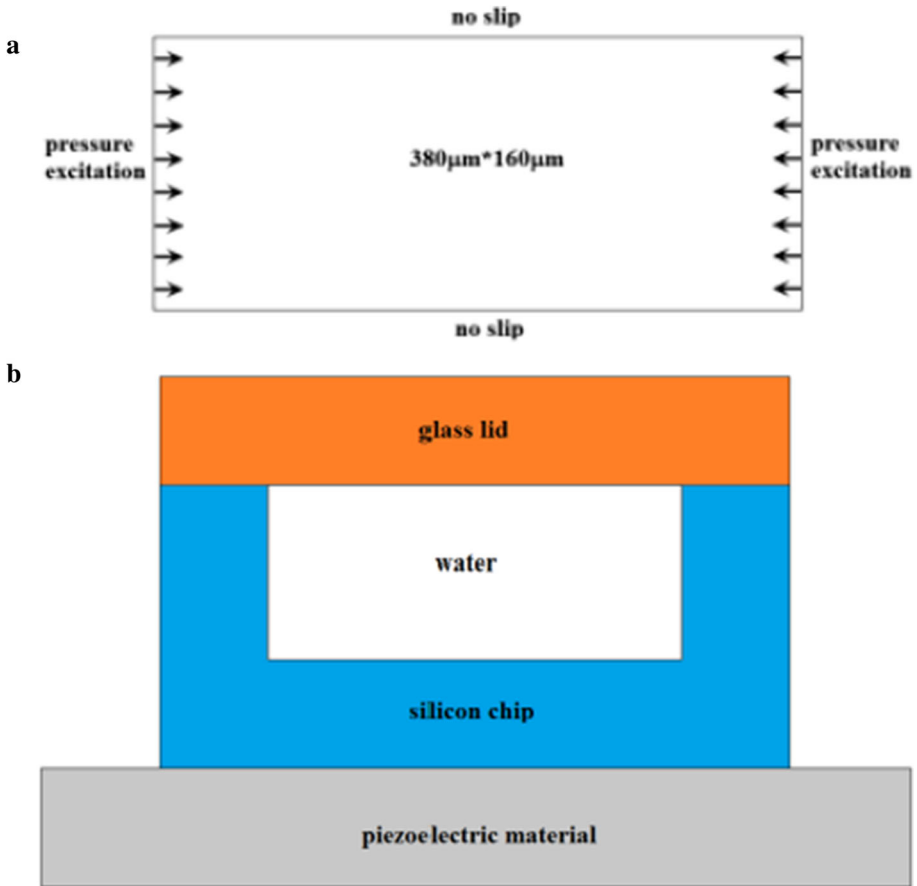


Fig. 1 Schematic diagram of **a** simplified and **b** full-sized models in the simulation of standing bulk acoustic wave in the microchannel

solid. On all outside boundaries, a free displacement was implemented (i.e., the Neumann boundary condition, $n \cdot \sigma_s = 0$). Both silicon and glass were all considered as linear elastic materials. An electrical potential of 20 V was applied to the PZT-5H plate for the acoustic excitation. All materials were from the built-in library of COMSOL. In order to obtain a relative convergence of the second-order velocity field, a maximum mesh size of $d_{\text{edge}} = 0.5\delta$ and $d_{\text{domain}} = 10\delta$ is required on the boundaries and in the domain, respectively [17]. There were in total 1.7×10^5 and 8.1×10^5 triangular elements and 7.3×10^5 and 8.4×10^6 degrees of freedom in the calculation of acoustic field using the simple model and full-sized model, respectively. The computation was performed on a Lenovo PC running Windows 10 system with 16 GB RAM and 3.4 GHz CPU.

2.2 SAW-induced acoustofluidics in the microchannel

A typical standing surface acoustic wave (SSAW) device for particle manipulation consists of a rectangular PDMS channel in the width of $600 \mu\text{m}$ and the height of $125 \mu\text{m}$ bonded on a piezoelectric lithium niobate (LiNbO_3) substrate. In the simplified model using impedance or

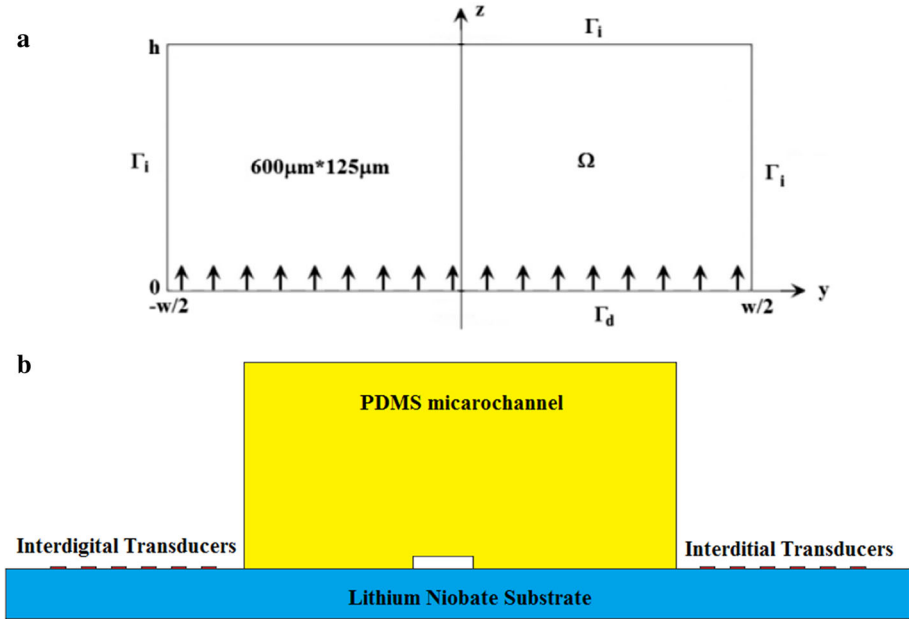


Fig. 2 Schematic diagram of **a** simplified or impedance boundary matching and **b** full-sized models in the simulation for standing surface acoustic wave in the microchannel

lossy-wall boundary conditions as shown in Fig. 2a, the boundaries of PDMS microchannel were denoted by Γ_i while the actuation boundary was denoted by Γ_d . The wavelength of SAW is $\lambda = 600 \mu\text{m}$ at the excitation frequency of 6.67 MHz. The SSAW displacement profile over Γ_d by superimposing the displacement profile of two SAWs traveling in opposite directions with a phase difference of $\Delta\phi$,

$$\begin{aligned}
 u_y(t, y) &= 0.6u_0e^{-C_d y} \left\{ \sin\left[k\left(\frac{W}{2} - x\right) + \omega t - \Delta\phi\right] + \sin\left[k\left(x - \frac{W}{2}\right) + \omega t\right] \right\} \\
 u_z(t, y) &= -u_0e^{-C_d y} \left\{ \cos\left[k\left(\frac{W}{2} - x\right) + \omega t - \Delta\phi\right] + \cos\left[k\left(x - \frac{W}{2}\right) + \omega t\right] \right\}
 \end{aligned}
 \tag{7}$$

where $C_d = 714 \text{ m}^{-1}$ is the decay coefficient at 6.67 MHz. At the interface of Γ_d , the boundary condition was

$$v_1(t, y) = \frac{\partial u(t, y)}{\partial t}
 \tag{8}$$

which assumes all transmitted wave energy to be absorbed in the PDMS materials. Such an assumption is generally valid for most of the microchannels in the applications with sufficient thickness (i.e., $> 1 \text{ mm}$) to attenuate all waves from the interface of PDMS and air. Meanwhile, the boundary condition on the channel walls with impedance condition was given by

$$n \cdot \nabla p_1 = i \frac{\omega \rho_0}{\rho_m c_m} p_1
 \tag{9}$$

where i is the imaginary unit, and ρ_m and c_m are the density and the speed of sound of the wall material, respectively.

In the full-sized model as shown in Fig. 2b, three pairs of IDTs in the electrode height of $20 \mu\text{m}$ were deposited on the LiNbO_3 substrate in the length of 9 mm and height of

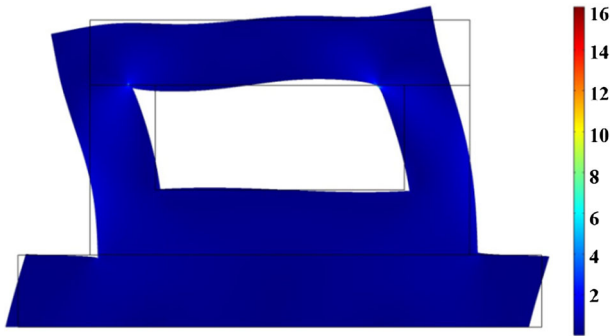


Fig. 3 Distribution of von Mises stress in MPa in the full-sized model

0.5 mm. All elements of the substrate were modeled as linear elastic materials, and an electrical potential of 40 V was applied to the IDTs for the SAW excitation. Both ends of the piezoelectric substrate had matched layers to prevent the reflection of SAWs. PDMS had a length of 4 mm and a height of 2.5 mm. The acoustic attenuation of the longitudinal wave in PDMS 10:1 was set as 22.4 dB/cm at 6.67 MHz extrapolated from the measured acoustic properties [4]. However, there were no measured data for the shear wave. The acoustic attenuation of the shear wave was assumed to be 3 times as high as that of the longitudinal wave in order to reduce the contribution of shear wave in the PDMS to the acoustic field inside the microchannel. At three outside PDMS boundaries, a free wall was implemented (i.e., $n \cdot \sigma_m = 0$). COMSOL modules of thermoacoustics, laminar flow, particle tracing, solid mechanics, and electrostatics were included with the coupling interfaces of the piezoelectric effect and thermoviscous acoustics-structure boundary. Coupling between the motion of walls and substrate and the flow model is described by the continuity conditions through the Cauchy model, $n \cdot \sigma_s = n \cdot \sigma_f$ and $\partial_t u = v$. Consistent stabilization with both streamline and crosswind diffusion was applied for the laminar flow module. Similarly, in order to obtain a relative convergence of the second-order velocity field, a maximum mesh size of $d_{\text{edge}} = 0.5\delta$ and $d_{\text{domain}} = 10\delta$ is required on the boundaries and in the domain, respectively [22]. There were in total 5.0×10^4 and 1.8×10^6 triangular elements and 1.2×10^6 and 3.9×10^8 degrees of freedom in the calculation of acoustic field using the simple model and full-sized model, respectively. Linear interpolation was applied for surface plot and data visualization.

3 Results

3.1 BAW-induced acoustofluidics

Using the full-sized model, the thickness shear mode produced by the PZT-5H piezoelectric material with the deformation in the horizontal direction is clearly illustrated (see Fig. 3). The elastic materials of silicon and glass also showed deformation with the response to the acoustic excitation. It is noted that the stress at the interface of the glass lid and top of the microchannel is larger than that at the bottom of the microchannel, which is similar to the previous finding [7]. The distributions of acoustic pressure, acoustic radiation force, streaming velocity, trajectory motion of 1 μm and 10 μm polystyrene microparticles in the microfluidic

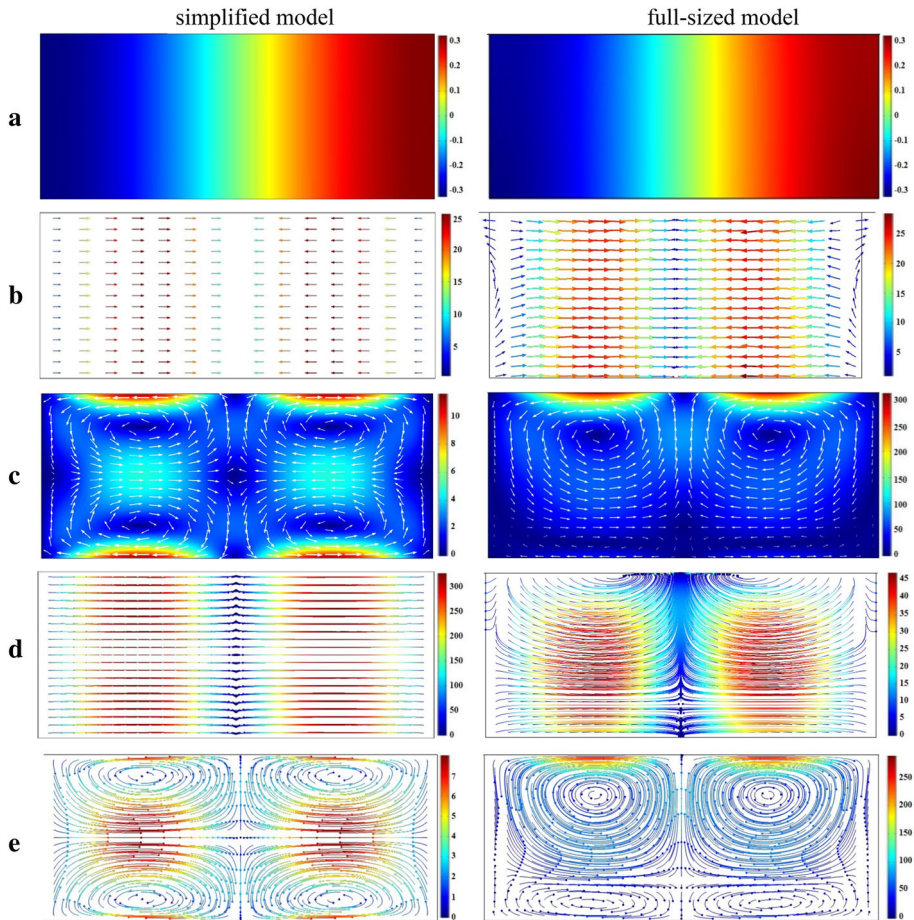


Fig. 4 Comparison of the distribution of **a** acoustic pressure in MPa, **b** acoustic radiation force in pN on $10\ \mu\text{m}$ polystyrene particle, **c** acoustic streaming velocity in $\mu\text{m/s}$, **d** motion of $10\ \mu\text{m}$ polystyrene particle in $\mu\text{m/s}$ at 1 s, and **e** motion of $1\ \mu\text{m}$ polystyrene particle in $\mu\text{m/s}$ at 10 s in the microchannel simulated by the simplified model after 10 s (left column) and full-sized model after 1 s (right column)

channel using the simplified and full-sized models are compared (Fig. 4). Characteristics are listed in Table 1. There are several findings. Firstly, the produced standing acoustic wave fields using these two models were similar. Secondly, although the distributions of acoustic radiation force in the central region of the microchannel are parallel to the top and bottom of the wall and similar in both simulations, those close to the side walls were curved slightly in the full-sized model. The patterns of acoustic radiation force for $1\ \mu\text{m}$ polystyrene microparticle were identical to those for $10\ \mu\text{m}$ ones (data not included) because the amplitude of acoustic force is proportional to a^3 according to Eq. (2). Thirdly, there were 4 symmetric Rayleigh streaming rolls in the simplified model. In comparison, the streaming pattern close to the top wall was more significant and larger than that close to the bottom wall in the full-sized model. The high acoustic streaming velocity, $311\ \mu\text{m/s}$, may be due to the significant deformation of the microfluidic channel. Finally, the corresponding trajectory motions of microparticles simulated using these two models were different. Acoustic radiation force dominates for large microparticles (i.e., $10\ \mu\text{m}$) while acoustic streaming for small ones (i.e., $1\ \mu\text{m}$). Previous

Table 1 Comparison of SBAW-induced acoustofluidic properties in the microchannel simulated using different models

	p (kPa)	$F_{\text{rad},10\ \mu\text{m}}$ (pN)	$F_{\text{rad},1\ \mu\text{m}}$ (fN)	v_{AS} ($\mu\text{m/s}$)	$v_{10\ \mu\text{m}}$ ($\mu\text{m/s}$)	$v_{1\ \mu\text{m}}$ ($\mu\text{m/s}$)
Simplified model	323	25.7	25.7	11.64	327.3	8.0
Full-sized model	323	31.8	31.8	311.7	472.2	287.4

p : acoustic pressure; $F_{\text{rad},10\ \mu\text{m}}$: acoustic radiation force on 10 μm polystyrene particle; $F_{\text{rad},1\ \mu\text{m}}$: acoustic radiation force on 1 μm polystyrene particle; v_{AS} : acoustic streaming velocity; $v_{10\ \mu\text{m}}$: trajectory velocity of 10 μm polystyrene particle; $v_{1\ \mu\text{m}}$: trajectory velocity of 1 μm polystyrene particle, all maximum values are listed in the table

studies showed a critical particle size for the transition between streaming-dominated and radiation-dominated motion is around 1–2 μm for the BAW system [17, 26]. It showed that 10 μm microparticles accumulated at the central line of microchannel using the simplified model while some of them were pushed to the upper sidewall and middle of the top wall using the full-sized model. Rolling of 1 μm microparticles related closely to acoustic streaming. Because of the high acoustic streaming velocity in the full-sized model, it took less time to form the Rayleigh streaming rolls in the microchannel.

Furthermore, the resonant performance of such a microfluidic channel using the full-sized model is shown in Fig. 5. The maximum acoustic pressure in the microchannel of 581.5 kPa was found at the frequency of 1.982 MHz, which is slightly different from the half-wavelength across the width of the microchannel. Its acoustophoresis patterns were similar to those at 1.97 MHz (Fig. S1). Therefore, the resonance of the cavity is usually measured with the impedance network for optimal performance. It is also shown that without the inclusion of thermoviscosity of fluid in the cavity the resonance was significantly different (Fig. S2). If the width of the microchannel is longer, more resonances with different patterns can be generated [20]. Furthermore, various actuation of piezoelectric transducers, such as different width of electrode and phase actuation applied to two electrodes [25], results in an easy adjustment of the generated acoustic field. The creation of “strip electrodes” is able to increase the number of resonance modes in a transducer and thereby actuate harmonics in the transversal resonator. Overall, the finite element method is proven as a useful tool in determining the location of resonant frequencies and understanding the resultant modes [20, 21].

3.2 SAW-induced acoustofluidics

The simulated SSAW-induced acoustophoresis using these two models with $\Delta\phi = \pi$ were compared (see Fig. 6), and their acoustophoresis characteristics are listed in Table 2. The vibration amplitude of SAW in the simplified model was set as $u_0 = 0.06$ nm. The acoustic pressures inside the microchannel were not set to match exactly with each other (but quite similar) as in the simulation of BAW because of different shapes of the generated acoustic standing wave fields. There are several differences between the simulation results. Firstly, the acoustic standing wave pattern in the full-sized model seemed shifted upwards slightly, which may be due to the reflected acoustic wave from the PDMS lid and deformation of the piezoelectric substrate. Secondly, significant deformation of the piezoelectric substrate produced large acoustic radiation force at the bottom of the microchannel to push large particles upwards. As a result, 10 μm polystyrene microspheres were accumulated at the middle

Fig. 5 The relationship of the maximum acoustic pressure in the microfluidic channel and the driving frequency of the piezoelectric substrate

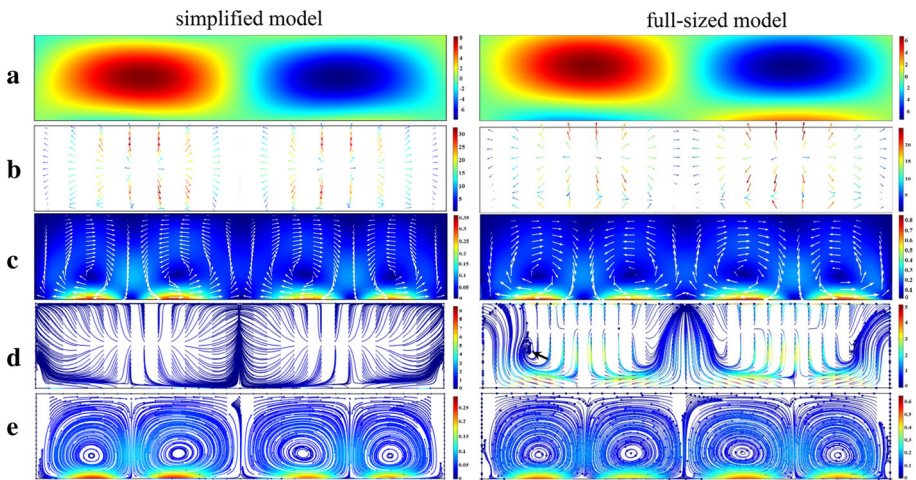
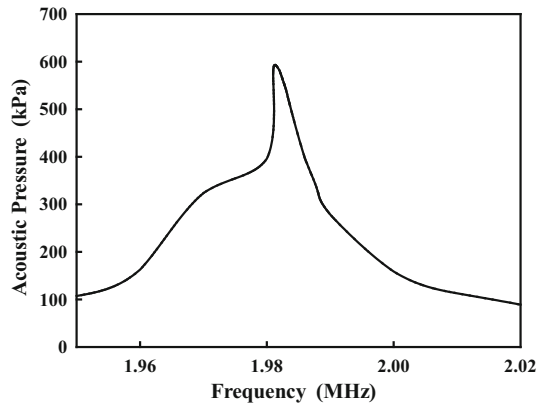


Fig. 6 Comparison of the distribution of **a** acoustic pressure in kPa, **b** acoustic radiation force in pN on $10\ \mu\text{m}$ polystyrene particle, **c** acoustic streaming velocity in $\mu\text{m/s}$, **d** motion of $10\ \mu\text{m}$ polystyrene particle in $\mu\text{m/s}$ at 200 s, and **e** motion of $1\ \mu\text{m}$ polystyrene particle in $\mu\text{m/s}$ at 200 s in the microchannel simulated by the simplified model (left column) and full-sized model (right column). Arrow shows a local vortex in the $10\ \mu\text{m}$ -particle motion

top of the microchannel. Finally, a local vortex may be formed. The acoustic attenuation of the longitudinal wave in the PDMS affects the magnitude and shape of the formed acoustic standing wave in the microchannel, but that of the shear wave has little influence because of higher attenuation (see Figs. S3 and S4). Furthermore, the acoustic fields of SSW at $\Delta\phi = -\pi/2, 0,$ and $\pi/2$ were also compared (see Fig. 7). The pressure node moved by a distance of $\lambda/8$ for each phase difference of $\pi/2$. However, the patterns of SSW simulated using the full-sized model seemed more similar to the shifted pattern from $\Delta\phi = -\pi$ by either shifting the IDTs or the PDMS microchannel.

Acoustophoretic trajectories of microparticles in the diameter of $0.5, 1.2, 5.2$ and $7.8\ \mu\text{m}$ along the PDMS microchannel cross section (a width of $600\ \mu\text{m}$ and a height of $125\ \mu\text{m}$) driven by standing SAWs excited from a pair of IDTs at the frequency of $6.166\ \text{MHz}$ and at peak-peak voltages of about $40\ \text{V}$ were obtained from the defocused particle images and then compared with the numerical prediction [2]. A good agreement was found between them

Table 2 Comparison of SSAW-induced acoustofluidic properties in the microchannel simulated using different models

	P^+ (kPa)	p^- (kPa)	$F_{\text{rad},10\mu\text{m}}$ (fN)	v_{AS} ($\mu\text{m/s}$)	$v_{10\mu\text{m}}$ ($\mu\text{m/s}$)	$v_{1\mu\text{m}}$ ($\mu\text{m/s}$)
Simplified model	8.17	- 7.83	32.8	0.36	9.58	0.29
Full-sized model	6.78	- 7.30	24.9	0.86	5.23	0.64

p^+ : positive acoustic pressure; p^- : negative acoustic pressure, all maximum values are listed in the table

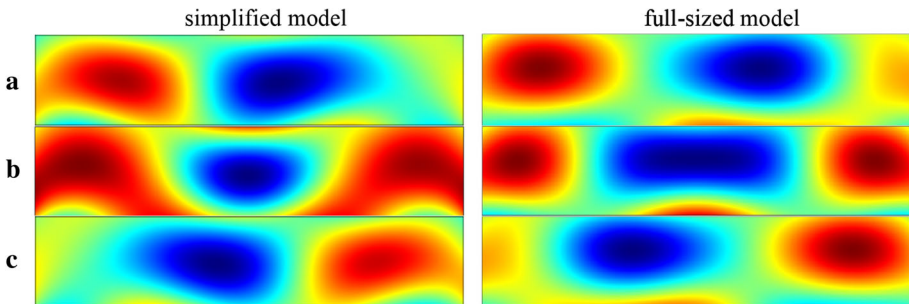


Fig. 7 Comparison of the acoustic pressure of standing surface acoustic waves inside the microchannel simulated by the simplified model (left column) and full-sized model (right column) with the phase difference of **a** $\Delta\phi = -\pi/2$, **b** $\Delta\phi = 0$, and **c** $\Delta\phi = \pi/2$

without any fitting parameter. Experimental data are of importance in validating the numerical models, including the full-sized model described here. Such a work will be carried out in the future research of acoustophoresis. That reduced-fluid model with the leaky impedance-wall condition included the Stokes drift with the use of the mean Lagrangian flow velocity using a time-scale separation approach rather than the usually employed Eulerian approaches [18]. Inclusion of Stokes drift [3, 19, 29] makes the prediction of microparticle trajectory more accurate and will also be available in the further evolution of the full-sized model.

4 Conclusions

In summary, two full-sized models were established to simulate the acoustophoresis in a silicon chip driven and excited by the bulk acoustic wave from a piezoelectric transducer and in a PDMS microchannel driven and excited by the surface acoustic wave propagating on the surface of a piezoelectric substrate, respectively. The distributions of acoustic pressure, acoustic radiation force, acoustic streaming, and trajectory motion of 1 μm and 10 μm polystyrene microparticles in the microchannel were simulated and compared with those using the simplified models. Significant differences were found between the models of BAW- and SAW-based system. The standing acoustic wave inside the fluidic cavity strongly influences the surrounding solid structure, and consequently, their interaction results in more significant and stronger acoustic streaming close to the solid wall. Both longitudinal and shear wave in the linear elastic solid affects the standing wave pattern and subsequently the microparticle motion. The full-sized models with the inclusion of all components and physical modules in the setup and practice would help to understand the response of the

acoustofluidic device and be very useful for the design and optimization process. Model validation using the experimental data and inclusion of Stokes drift are required in the future work.

Acknowledgements This work was supported by the Academic Research Fund (AcRF Tier 1, RG47/18), Ministry of Education, Singapore.

Data Availability Statement This manuscript has associated data in a data repository. [Authors' comment: All data included in this manuscript are available upon request contacting with the corresponding author.]

Authors' contribution In this work, Dr. Zhou made the simulation, performed data analysis, and wrote the manuscript.

Compliance with ethical standards

Conflict of interest The author declares no conflicts of interest. Also, the funding sponsor had no role in the design of the study, the collection, analyses or interpretation of data, nor in the writing of the manuscript and in the decision to publish the results.

References

1. M. Antfolk, C. Magnusson, P. Augustsson, H. Lilja, T. Laurell, Acoustofluidic, label-free separation and simultaneous concentration of rare tumor cells from white blood cells. *Anal. Chem.* **87**, 9322–9328 (2015). <https://doi.org/10.1021/acs.analchem.5b02023>
2. R. Barnkob, N. Nama, L. Ren, T.J. Huang, F. Costanzo, C.J. Kähler, Acoustically driven fluid and particle motion in confined and leaky systems. *Phys. Rev. Appl.* **9**, 014027 (2018). <https://doi.org/10.1103/PhysRevApplied.9.014027>
3. O. Bühler, *Waves and Mean Flows* (Cambridge University Press, Cambridge, 2011)
4. A. Cafarelli, A. Verbeni, A. Poliziani, P. Dario, A. Menciassi, L. Ricotti, Tuning acoustic and mechanical properties of materials for ultrasound phantoms and smart substrates for cell cultures. *Acta Biomater.* **49**, 368–378 (2017). <https://doi.org/10.1016/j.actbio.2016.11.049>
5. X. Ding, P. Li, S.-C.S. Lin, Z.S. Stratton, N. Nama, F. Guo, D. Slotcavage, X. Mao, J. Shi, F. Costanzo, Surface acoustic wave microfluidics. *Lab Chip* **13**, 3626–3649 (2013). <https://doi.org/10.1039/C3LC50361E>
6. X. Ding, Z. Peng, S.-C.S. Lin, M. Geri, S. Li, P. Li, Y. Chen, M. Dao, S. Suresh, T.J. Huang, Cell separation using tilted-angle standing surface acoustic waves. *Proc. Natl. Acad. Sci.* **111**, 12992–12997 (2014). <https://doi.org/10.1073/pnas.1413325111>
7. J. Dual, T. Schwarz, Acoustofluidics 3: continuum mechanics for ultrasonic particle manipulation. *Lab Chip* **12**, 244–252 (2012). <https://doi.org/10.1039/9781849737067-00046>
8. T. Franke, S. Braunmüller, L. Schmid, A. Wixforth, D. Weitz, Surface acoustic wave actuated cell sorting (SAWACS). *Lab Chip* **10**, 789–794 (2010). <https://doi.org/10.1039/B915522H>
9. L.P. Gor'kov, On the forces acting on a small particle in an acoustic field in an ideal fluid. *Sov. Phys. Dokl.* **6**, 773–775 (1962)
10. N. Harris, M. Hill, S. Beeby, Y. Shen, N. White, J. Hawkes, W. Coakley, A silicon microfluidic ultrasonic separator. *Sens. Actuat. B Chem.* **95**, 425–434 (2003). [https://doi.org/10.1016/s0925-4005\(03\)00448-9](https://doi.org/10.1016/s0925-4005(03)00448-9)
11. H. Jönsson, C. Holm, A. Nilsson, F. Petersson, P. Johnsson, T. Laurell, Particle separation using ultrasound can radically reduce embolic load to brain after cardiac surgery. *Ann. Thorac. Surg.* **78**, 1572–1577 (2004). <https://doi.org/10.1016/j.athoracsur.2004.04.071>
12. M. Koklu, A.C. Sabuncu, A. Beskok, Acoustophoresis in shallow microchannels. *J. Colloid Interface Sci.* **351**, 407–414 (2010). <https://doi.org/10.1016/j.jcis.2010.08.029>
13. I. Leibacher, P. Reichert, J. Dual, Microfluidic droplet handling by bulk acoustic wave (BAW) acoustophoresis. *Lab Chip* **15**, 2896–2905 (2015). <https://doi.org/10.1039/c5lc00083a>
14. A. Lenshof, M. Evander, T. Laurell, J. Nilsson, Acoustofluidics 5: building microfluidic acoustic resonators. *Lab Chip* **12**, 684–695 (2012). <https://doi.org/10.1039/c1lc20996e>

15. Z. Mandralis, D. Feke, W. Bolek, W. Burger, E. Benes, Enhanced synchronized ultrasonic and flow-field fractionation of suspensions. *Ultrasonics* **32**, 113–122 (1994). [https://doi.org/10.1016/0041-624x\(94\)90019-1](https://doi.org/10.1016/0041-624x(94)90019-1)
16. Z.I. Mandralis, D.L. Feke, Continuous suspension fractionation using acoustic and divided-flow fields. *Chem. Eng. Sci.* **48**, 3897–3905 (1993). [https://doi.org/10.1016/0009-2509\(93\)80368-z](https://doi.org/10.1016/0009-2509(93)80368-z)
17. P.B. Muller, R. Barnkob, M.J.H. Jensen, H. Bruus, A numerical study of microparticle acoustophoresis driven by acoustic radiation forces and streaming-induced drag forces. *Lab Chip* **12**, 4617–4627 (2012). <https://doi.org/10.1039/c2lc40612h>
18. N. Nama, R. Barnkob, Z. Mao, C.J. Kähler, F. Costanzo, T.J. Huang, Numerical study of acoustophoretic motion of particles in a PDMS microchannel driven by surface acoustic waves. *Lab Chip* **15**, 2700–2709 (2015). <https://doi.org/10.1039/C5LC00231A>
19. N. Nama, T.J. Huang, F. Costanzo, Acoustic streaming: an arbitrary Lagrangian–Eulerian perspective. *J. Fluid Mech.* **825**, 600–630 (2017). <https://doi.org/10.1017/jfm.2017.338>
20. A. Neild, S. Oberti, J. Dual, Design, modeling and characterization of microfluidic devices for ultrasonic manipulation. *Sens. Actuat. B Chem.* **121**, 452–461 (2007). <https://doi.org/10.1016/j.snb.2006.04.065>
21. A. Neild, S. Oberti, A. Haake, J. Dual, Finite element modeling of a microparticle manipulator. *Ultrasonics* **44**, e455–e460 (2006). <https://doi.org/10.1016/j.ultras.2006.05.168>
22. Z. Ni, C. Yin, G. Xu, L. Xie, J. Huang, S. Liu, J. Tu, X. Guo, D. Zhang, Modelling of SAW-PDMS acoustofluidics: physical fields and particle motions influenced by different descriptions of the PDMS domain. *Lab Chip* **19**, 2728–2740 (2019). <https://doi.org/10.1039/C9LC00431A>
23. F. Petersson, L. Åberg, A.-M. Swärd-Nilsson, T. Laurell, Free flow acoustophoresis: microfluidic-based mode of particle and cell separation. *Anal. Chem.* **79**, 5117–5123 (2007). <https://doi.org/10.1021/ac070444e>
24. F. Petersson, A. Nilsson, C. Holm, H. Jönsson, T. Laurell, Separation of lipids from blood utilizing ultrasonic standing waves in microfluidic channels. *Analyst* **129**, 938–943 (2004). <https://doi.org/10.1039/B409139F>
25. F. Petersson, A. Nilsson, C. Holm, H. Jönsson, T. Laurell, Continuous separation of lipid particles from erythrocytes by means of laminar flow and acoustic standing wave forces. *Lab Chip* **5**, 20–22 (2005). <https://doi.org/10.1039/B405748C>
26. M. Settnes, H. Bruus, Forces acting on a small particle in an acoustical field in a viscous fluid. *Phys. Rev. E* **85**, 016327 (2012). <https://doi.org/10.1103/PhysRevE.85.016327>
27. N. Skov, H. Bruus, Modeling of microdevices for SAW-based acoustophoresis—a study of boundary conditions. *Micromachines* **7**, 182 (2016). <https://doi.org/10.3390/mi7100182>
28. F.J. Trujillo, P. Juliano, G. Barbosa-Canovas, K. Knoerzer, Separation of suspensions and emulsions via ultrasonic standing waves—a review. *Ultrason. Sonochem.* **21**, 2151–2164 (2014). <https://doi.org/10.1016/j.ultsonch.2014.02.016>
29. J. Vanneste, O. Bühler, Streaming by leaky surface acoustic waves. *Proc. R. Soc. A* **467**, 1779–1800 (2011). <https://doi.org/10.1098/rspa.2010.0457>
30. M. Wu, P.H. Huang, R. Zhang, Z. Mao, C. Chen, G. Kemeny, P. Li, A.V. Lee, R. Gyanchandani, A.J. Armstrong, Circulating tumor cell phenotyping via high-throughput acoustic separation. *Small* **14**, 1801131 (2018). <https://doi.org/10.1002/sml.201801131>
31. M. Wu, A. Ozcelik, J. Rufo, Z. Wang, R. Fang, T.J. Huang, Acoustofluidic separation of cells and particles. *Microsyst. Nanoeng.* **5**, 32 (2019). <https://doi.org/10.1038/s41378-019-0064-3>